Design and test of an *X*-band constant gradient structure

Qiang Gao, Hao Zha, Jiaru Shi,* Xiancai Lin, Yingchao Du, Boyuan Feng, Hongyu Li, Heng Deng, Fangjun Hu, Jian Gao, Qingzhu Li, Weihang Gu, Jiayang Liu, Wenhui Huang, Chuanxiang Tang, and Huaibi Chen

Department of Engineering Physics, Tsinghua University, Beijing 100084, China
and Key Laboratory of Particle and Radiation Imaging, Tsinghua University,
Ministry of Education, Beijing 100084, China

(Received 21 April 2024; accepted 1 August 2024; published 6 September 2024)

A light source project named very compact inverse Compton scattering gamma-ray source (VIGAS) is under development at Tsinghua University. VIGAS aims to generate monochromatic high-energy gamma rays by colliding 350-MeV electron beams with 400-nm laser photons within a 12-m beamline. To produce a high-energy electron beam in such a compact space, the system consists of an S-band high-brightness injector and six X-band high-gradient accelerating structures. The goal of the X-band structure is to operate at a high gradient of 80 MV/m. Therefore, we adopts the constant gradient traveling wave approach, where the iris from the first cell to the end cell is tapered. The structure has 72 cells, including 70 cells and 2 couplers, so we named it XT72. The frequency of XT72 is selected to 11.424 GHz, and the $2\pi/3$ mode is adopted. In this paper, we present a comprehensive study covering the detailed design, fabrication, rf tuning, and high-power test results of the first XT72. Additionally, we compare the performance of this structure to that of the previous constant impedance structure. Our results demonstrate that the XT72 is capable of operating at an 80-MV/m gradient with a lower breakdown rate. This advancement paves the way for the development of VIGAS project and contributes to the wider application of X-band room-temperature high-gradient structures in compact accelerator facilities.

DOI: 10.1103/PhysRevAccelBeams.27.090401

I. INTRODUCTION

High brightness, monochromatic, and tunable x-ray sources have wide applications in many fields, such as production of medical radioisotopes and protein crystallography [1,2], isotope-selective radiography and material assay [3,4], and radiation therapy and cultural heritage preservation [5,6]. Therefore, there is a growing need for advanced light source tools or facilities. One promising method to generate a high-bright and monochromatic photons is the inverse Compton scattering (ICS), which involves a scheme where a high-intensity laser is scattered from high-energy electrons, resulting in the transformation of laser photons into x-ray photons due to the Doppler shift [7]. Many facilities aimed at generating high-energy and high-flux gamma-rays are being developed, for example, the ThomX ICS source (45–90 keV, 10^{12}–10^{13} ph/s) at IJCLAB in Orsay [8], the compact light source (15–35 keV, 10^{10}–10^{11} ph/s) of Lyncean Technologies in Munich [9,10], the extreme-light-infrastructure nuclear-physics gamma-beam-source project (ELI-NP-GBS, 0.2 to 20 MeV, 10^8 ph/s) in Romania [11,12], and Tsinghua Thomson Scattering X-ray Source (TTX, 50 keV, 10^7 ph/s) at Tsinghua University in Beijing [13–15].

Recently, Tsinghua University has proposed a program to develop a very compact inverse Compton scattering gamma-ray source (VIGAS), the goal of VIGAS is to generate a high flux gamma rays of 10^8 ph/s with continuously adjustable energy in the range of 0.2–4.8 MeV by colliding an electron bunch with a 400- or 800-nm laser, the electron's energy can be tuned from 50 to 350 MeV and the emittance is less than 0.6 μm [16–18]. Currently, the beamline is under construction and we expect to achieve the first light by the end of 2025.

The beamline 3D model and schematics are illustrated in Figs. 1(a) and 1(b), with all elements abbreviations listed in the table below. The length from photoinjector cathode to the electron-laser interaction point is less than 12 m, while the total length including the electron beam energy diagnostic system is about 14 m. The entire beamline can be divided into two sections: the S-band high-brightness injector section and the X-band main accelerator section. The S-band injector section comprises an S-band photoinjector [19] and a traveling wave structure [20] powered by a Canon E3730A 50-MW klystron. Additionally, there

*Contact author: shij@tsinghua.edu.cn

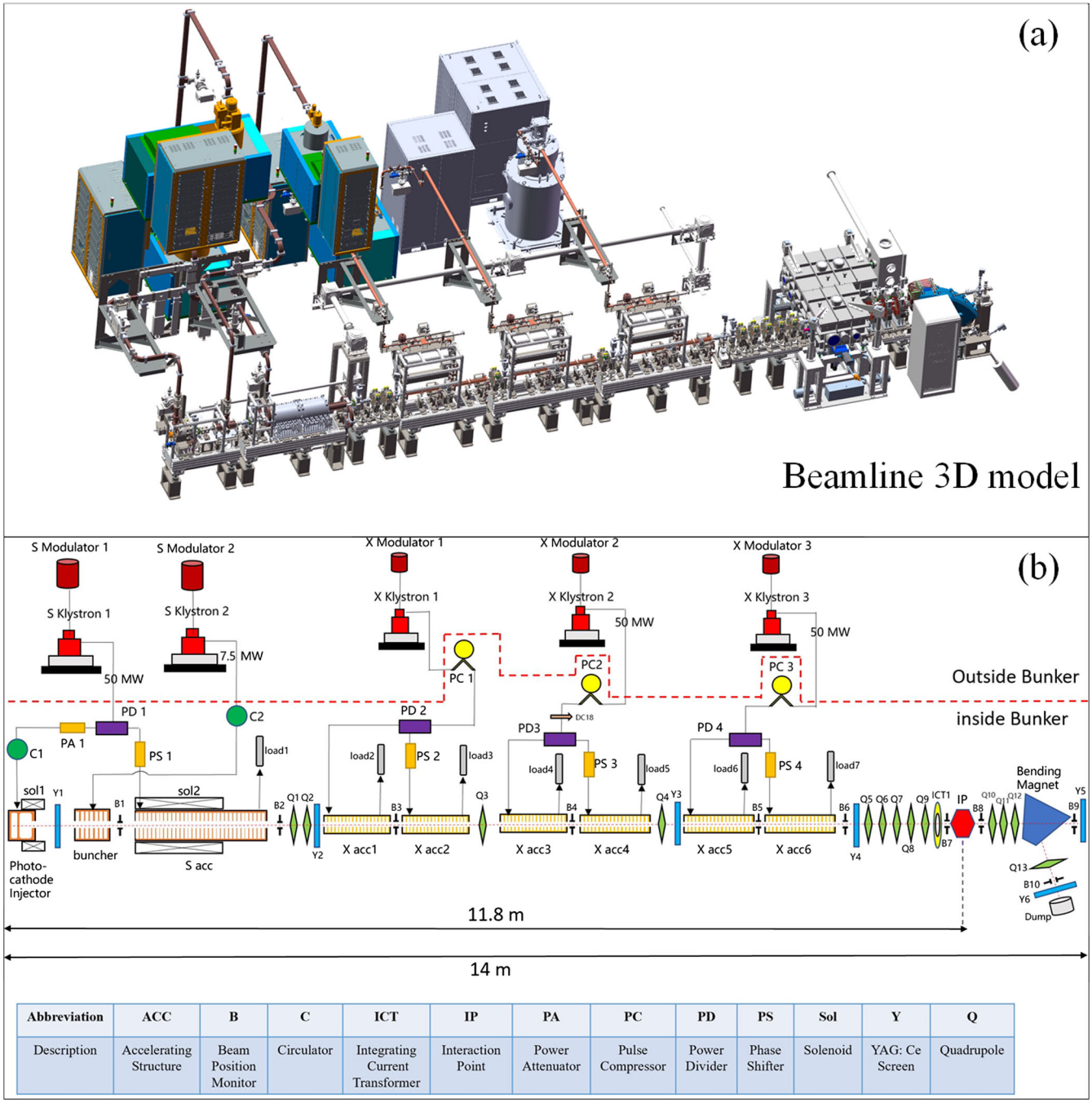

Abbreviation	ACC	B	C	ICT	IP	PA	PC	PD	PS	Sol	Y	Q
Description	Accelerating Structure	Beam Position Monitor	Circulator	Integrating Current Transformer	Interaction Point	Power Attenuator	Pulse Compressor	Power Divider	Phase Shifter	Solenoid	YAG: Ce Screen	Quadrupole

FIG. 1. VIGAS beamline layout. (a) Beamline 3D model. (b) Schematic and main elements description.

is a S-band 7-cell standing wave buncher located between the photoinjector and the accelerating structure. Its purpose is to compress the bunch length and it is powered by another 7.5-MW klystron. The photoinjector solenoid sol 1 and S-band traveling-wave accelerating structure solenoid sol 2 serve as the focusing elements and play roles in emittance compensation [21]. The X-band main accelerator section comprises three identical modules, each consisting of a 50-MW X-band klystron, a pulse compressor, and two high-gradient X-band accelerating structures. The pulse compressor serves to increase the peak power of the rf while compressing the pulse length. Subsequently, the compressed rf pulse is split and fed into two structures. At the end of the S-band injector, the electron bunch energy is approximately 50 MeV. Each X-band accelerating structure provides an energy gain of 50 MeV, enabling the total electron energy at the end of the X-band main accelerator section to reach 350 MeV.

The goals of VIGAS for an X-band high-gradient structure are to achieve a gradient of at least 80 MV/m and an energy gain of at least 50 MeV, resulting in a structure length of no less than 0.63 m. The repetition rate

of VIGAS is 10 Hz, which means the break down rate (BDR) should not exceed 2×10^{-5}/pulse in order to avoid break down during 1 h of continuous operation. According to the conditioning history of X-band structures in CERN and KEK, it will take more than 10^8 pulses of conditioning to achieve a low BDR of 10^{-6}/pulse/m [22]. However, considering that VIGAS requires six X-band structures within 2 years, we have decided to condition each structure up to 20 millions pulses in high-power test, aiming to achieve 80 MV/m gradient with BDR at the level of 10^{-4}/pulse for time saving.

Given the fact that X-band structures can achieve higher accelerating gradients and are more compact compared to lower frequency bands structures [23], many light source facilities adopt X-band structures as part of their accelerator systems. For instance, the CERN CLIC program operates X-band accelerating structures at 100 MV/m, subsequently, the collaboration between CERN, KEK, and Tsinghua University push the limit to 120 MV/m by a choke mode damped structure [24,25]. Additionally, the EuPRAXIA program at SPARC LAB is developing an X-band linac with a gradient of 57 or 80 MV/m [26]. Moreover, the Shanghai Institute of Applied Physics has designed an X-band accelerating structure with a target gradient of 80 MV/m for its compact hard X-ray FEL program [27].

Due to convenience in fabrication, we initially adopted a constant impedance (CI) approach. In 2021, we developed a prototype of a CI X-band traveling wave structure with 72 cells, which we named XC72 (X-band constant impedance structure with **72** cells) [28]. XC72 underwent conditioning for nearly 20 million pulses. Although XC72 has reached almost 80 MV/m, the BDR is about 10^{-3}/pulse m, slightly higher than we required, mostly because the field in the first cell is too high. Therefore, we decided to switch to the constant gradient (CG) approach. The CG structure has the same number of cells as XC72, but the apertures are tapered from input to output, thus we name it XT72 (X-band tapered structure with 72 cells).

In this paper, we present the fully detailed design of XT72, along with the fabrication, rf tuning, and high-power test results of the first XT72 structure. The results demonstrate its ability to operate at a gradient of 80 MV/m with a lower BDR.

The paper is organized as follows: First, we introduce the physics design, including the rf design, coupler optimization, and wakefields effect analysis. Second, we illustrate the fabrication and rf tuning process of the first XT72 structure to validate the physics design. In the last section, we present the high-power test results and analysis, with the comparison to those of XC72.

II. PHYSICS DESIGN

This section is divided into three subsections. In the first part, we introduce the rf design of a single cell and the entire structure, including a comparison of the main rf characteristics with XC72. In the second section, we present the coupler optimization, particularly on the suppression of multipole fields from couplers. Lastly, we provide a method to calculate the wake function of the structure and a quantitative analysis of the wakefields effect on beam dynamics.

A. rf design

The CPI VKX8311B X-band klystron is selected as our power source, which could generate 50-MW and 1.5 μs pulsed power with a maximum repetition rate of 40 Hz. In order to drive two X-band accelerating structures in one module as shown in Fig. 1, a pulse compressor (PC) has to be implemented. The quality factor of the PC is designed to be 90 000 with a coupling factor of 3.5, it can compress the pulse length by a factor of 10 and boost the power by a factor of 5. Therefore, the filling time of the structure should be not exceeding 150 ns with the shunt impedance of the structure greater than 90 MΩ/m. Similar as the design of XC72 stated in Ref. [28], we choose $2\pi/3$ phase advance per cell as the working mode for a better trade-off between shunt impedance and filling time. The aperture of the cell is a crucial variable; the smaller it is, the higher the shunt impedance and longer the filling time, but the wakefield is more intense. The apertures of the CG structure are selected to be in the range of 3.92 to 3.12 mm, resulting in an average aperture of 3.52 mm, which is similar to that of XC72.

Table I presents the crucial rf properties of the first, middle, and end cell. The v_g/c denotes the group velocity relative to the speed of light, r/Q represents the shunt impedance over quality factor, E_s denotes the surface electric field, E_a represents the accelerating gradient of the cell, H_s denotes the surface magnetic field, and S_c is the modified Poynting factor [29,30], which can be expressed by

$$\begin{cases} Sc = |\mathrm{Re}(\vec{S})| + \frac{1}{6}|\mathrm{Im}(\vec{S})| \\ \vec{S} = \frac{1}{2}\vec{E} \times \vec{H}^* \end{cases}. \tag{1}$$

Figure 2 shows the distribution of surface electric field, magnetic field, and modified Poynting factor in the first,

TABLE I. rf properties of the first, middle, and end cell.

Properties	First cell	Middle cell	End cell
Aperture radius (mm)	3.92	3.52	3.12
Frequency (GHz)	11.424	11.424	11.424
Quality factor	7056	7024	6996
v_g/c (%)	3.20	2.23	1.44
r/Q (Ω/m)	13261	14404	15650
E_s/E_a	2.06	1.99	1.96
H_s/E_a (mA/V)	2.85	2.75	2.66
S_c/Ea^2 (mA/V)	0.52	0.44	0.35

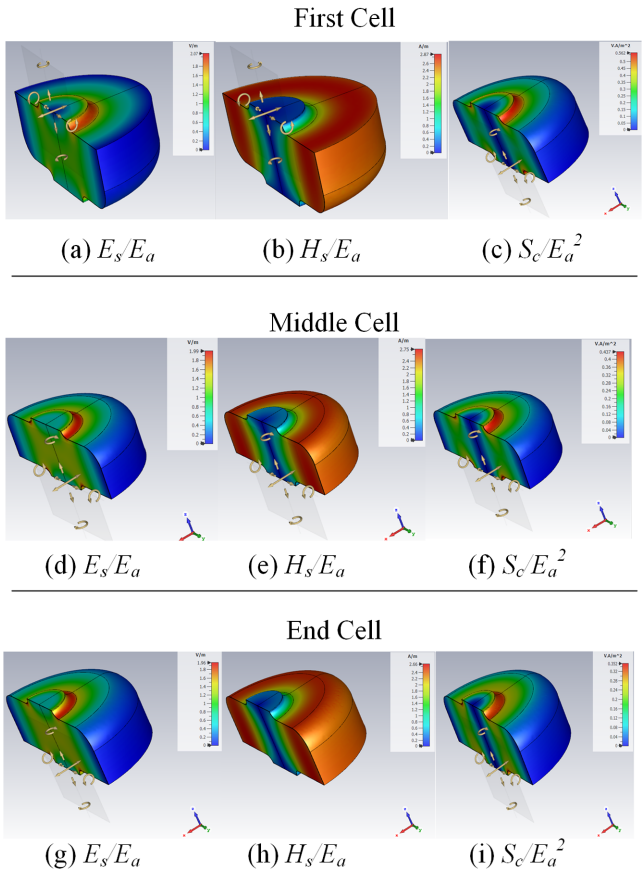

FIG. 2. First, middle, and end single cell rf surface electric field, magnetic field, and modified Poynting factor in simulation.

middle, and end cells, as simulated using CST Studio Suite®. The parameters of the other cells can be interpolated using the data from the first, middle, and end cells. The rf properties of the entire structure are listed in Table II, with a comparison to XC72. Using the data in Table II, we can calculate the output power required from the pulse compressor for XT72 to achieve 80 MV/m by the method in Ref. [31], as shown in Fig 3. The blue line is the power incident into the power compressor, the total pulse length is 1.2 μs, with a phase reverse at 1.1 μs. The quality of the PC is 90 000 with coupling coefficient of 3.5, thus the output power from PC is a factor of 5 to the incident power, but only 100 ns pulse length, as indicated by the red line. The

TABLE II. rf properties of the XT72 and XC72.

Properties	XT72 (CG)	XC72 (CI)
Aperture radius (mm)	3.92–3.12	3.50
Frequency (GHz)	11.424	11.424
Quality factor	7056–6996	7020
v_g/c (%)	3.20–1.44	2.2
Shunt impedance (MΩ/m)	93–109	101
Filling time (ns)	98	94
Working mode	$2\pi/3$	$2\pi/3$

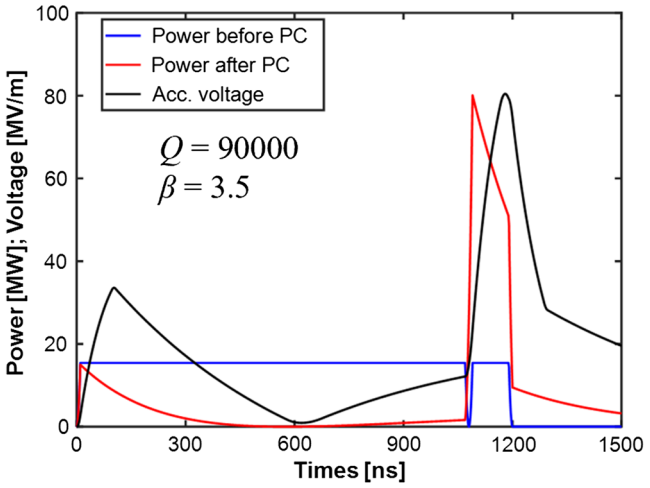

FIG. 3. Numerical calculation results of required power and gradient in time domain.

gradient in time domain of XT72 can be numerically calculated using the following equation:

$$G(t) = \int_0^L \sqrt{\frac{\omega r(z) P[t-\tau(z)]}{v_g(z) Q(z)}} e^{-\alpha(z)} H[t-\tau(z)] dz, \qquad (2)$$

where $P(t)$ is the structure incident power, $\alpha(z) = \frac{1}{2}\int_0^z \frac{\omega}{v_g(z')Q(z')} dz'$ denotes the power attenuation factor along the structure, $\tau(z) = \int_0^z \frac{dz'}{v_g(z')}$ represents the signal time delay, and $H(t-\tau)$ is the heavyside function. Substituting the input power (red line in Fig. 3) and rf properties of each cell in Table II into Eq. (2), the gradient in time domain can be derived as shown by the black line in Fig. 3. From this calculation, the required peak power out of the PC is 80 MW in order to achieve gradient of 80 MV/m. It should be noted that for the CG structure, the optimal pulse shape is square, rather than the exponentially decaying shape from a pulse compressor. Therefore, if a pulse with a longer flat-top is used, the required power should be less than 80 MW.

Maximum surface electric field, surface magnetic field, and modified Poynting factor are three important physical quantities that can affect BDR. To have a as low BDR as 10^{-6}/(pulse m), there are empirical thresholds of these quantities. According to the experiment results from CERN and KEK [22,30,32], a good criteria for the surface electric field in design is not to exceed 210 MV/m and for the modified Poynting factor, it should be less than 5 MW/mm^2. The surface magnetic field mainly causes pulsed heating, especially in the couplers of the structure. For copper, the equation to estimate the pulsed heating effect can be written as Eq. (3) [33,34]

$$\Delta T = 127 |H_\parallel|^2 \sqrt{f t_p}, \qquad (3)$$

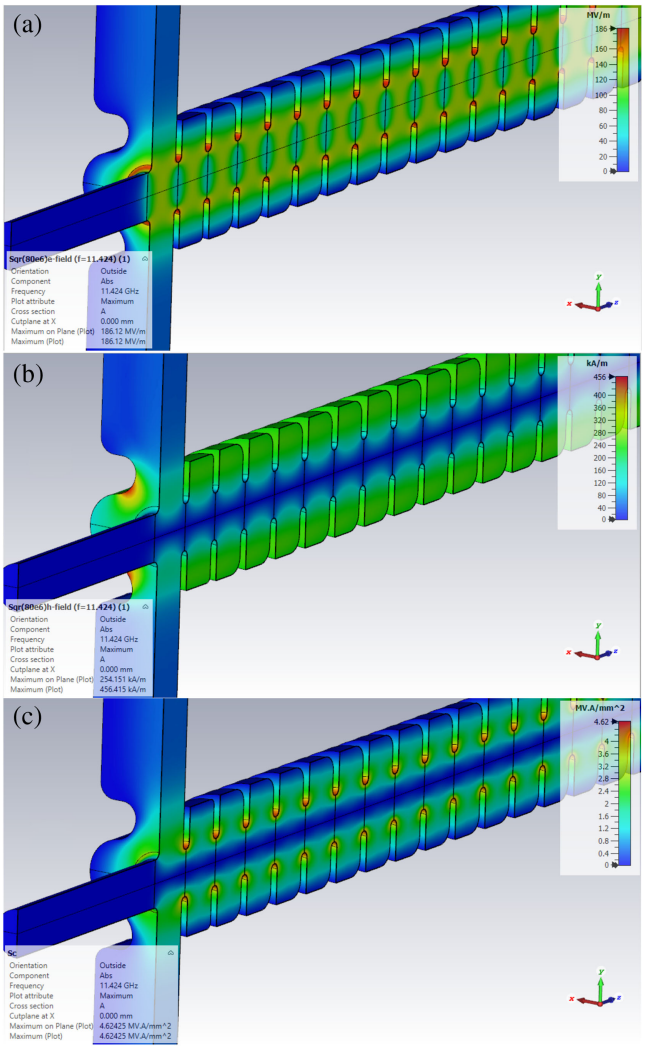

FIG. 4. (a) Surface electric field E_s, (b) surface magnetic field H_s, and (c) modified Poynting factor S_c at 80 MW of incident power simulation results from CST Studio Suite®.

where $H_{\|}$ is the maximum surface magnetic field in MA/m, f is the rf frequency in GHz, and t_p is the pulse length in μs. A practical criteria from experiment is that the temperature rising due to pulsed heating should be less than 50 °C [35,36]. In our case, the rf pulse length incident to the structure is around 100 ns, thus the maximum surface magnetic field should not exceed 610 kA/m according to Eq. (3).

To evaluate the design performance, the entire structure model is built and simulated using CST Studio Suite® F-solver to calculate surface electric field, surface magnetic field, and modified Poynting factor, as shown in Fig. 4. All the quantities are scaled in accordance with 80 MW input power, which generates 80 MV/m gradient. The values are listed in Table III along with the comparison with XC72 and recommended design thresholds.

Table III concludes that the design of XT72 meets with the empirical threshold values. Additionally, all critical physical quantities that affect BDR are improved compared to XC72, except H_s. The reason for a larger H_s is that XT72 adopts a racetrack coupler to suppress the emittance growth due to multipole fields, which is presented in detail in the next section.

TABLE III. Comparison of XT72, XC72, and recommended design thresholds on maximum surface electric field E_s, surface magnetic field H_s, and modified Poynting factor S_c.

Properties	XT72 (CG)	XC72 (CI)	Thresholds
E_s (MV/m)	186	224	<210
H_s (kA/m)	456	383	<610
S_c (MW/mm^2)	4.62	5.65	≤5

B. Coupler optimization

The dual-feed coupler approach is adopted for XT72 as illustrated in Fig. 4, in which the dipole field component effect in the coupler can be mitigated. However, there is still quadrupole field component inside which could deteriorate the emittance during the electron acceleration [37]. One method to suppress this effect is by using a racetrack coupler. The geometry of this type of coupler consists of two circles with a distance Δ_x between them. Three kinds of coupler schematics and their characteristics are depicted in Fig. 5.

By adjusting the separation distance Δx between two cylinders in the coupler, the quadrupole field component can be optimized to the minimum value. The small reflection S_{11} could be obtained by adjusting the coupler radius. The method to evaluate the high-order fields component can be described as follows. First, draw a circle with a radius of 2 mm at the center of the coupler, as indicated by the blue line in Fig. 6. Next, calculate the tangential magnetic field H_φ along the circle. Finally, analyze the multipole field components from the field distribution by using Fourier transformation. The fields H_φ

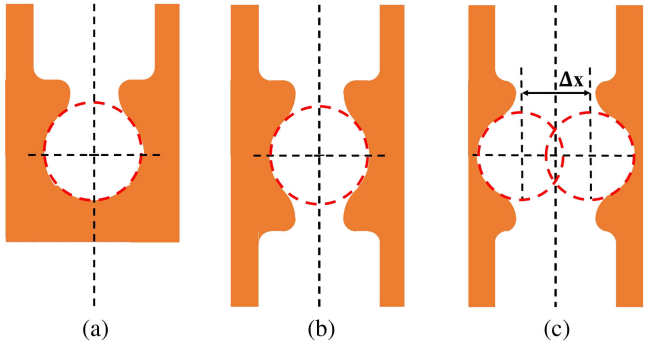

FIG. 5. (a) Single port coupler, with strong dipole and quadrupole field components. (b) Dual-feed regular coupler, with strong quadrupole field component. (c) Dual-feed coupler with racetrack geometry, both dipole and quadrupole field components can be suppressed.

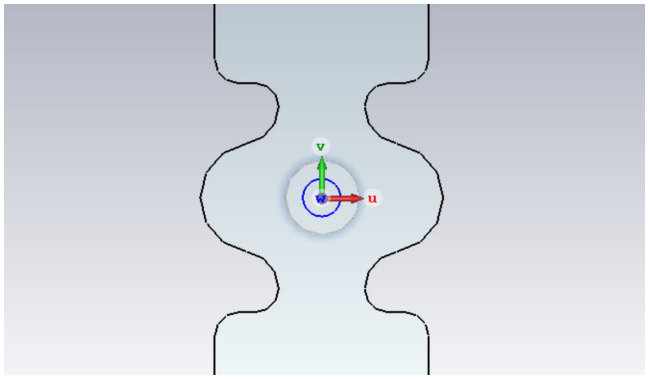

FIG. 6. Cross-sectional view of the coupler: The blue circle represents a virtual geometry used to evaluate fields on it.

in a dual-feed regular coupler and racetrack coupler are shown in Fig. 7. From this, one can see that the quadrupole field component dominates in the regular coupler, while the octopole field is the main component in racetrack coupler.

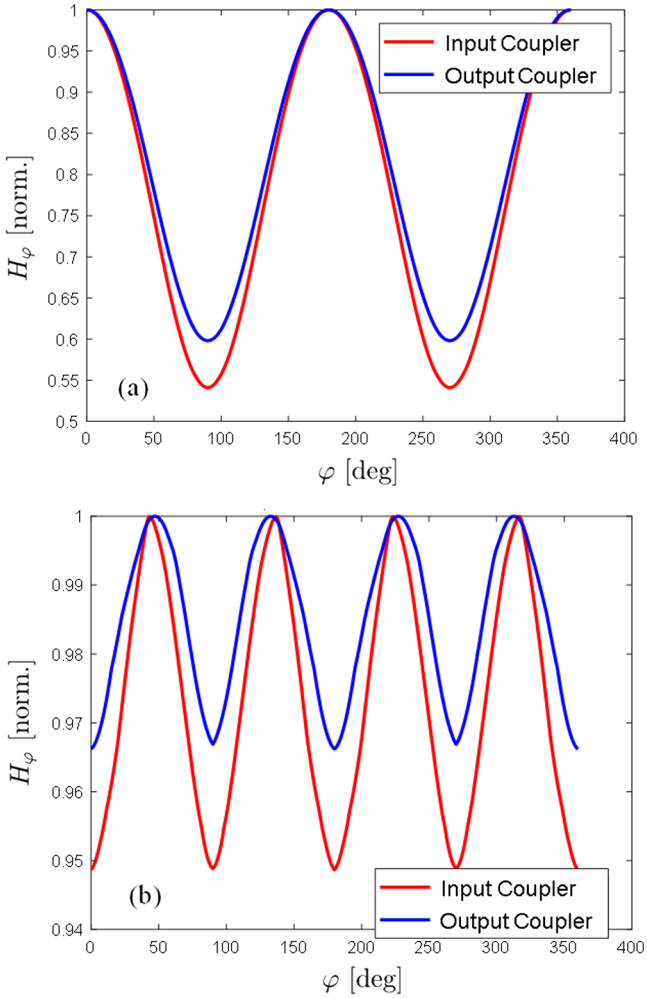

FIG. 7. Normalized field H_φ in the regular coupler (a) and in the racetrack coupler (b) along a circle in the coupler center.

TABLE IV. Comparison of quadrupole field component strength relative to the monopole field component in regular and racetrack coupler.

	Relative strength	
Coupler type	Input coupler	Output coupler
Regular	0.29	0.25
Racetrack	8×10^{-4}	1×10^{-3}

The Fourier transformation is applied on the data in Fig. 7, and the quadrupole field components strength relative to the monopole field are calculated and listed in Table IV. The calculation results indicate that the quadrupole field strength is suppressed by 2–3 orders of magnitude as compared with the circular coupler shape.

The disadvantage of adopting racetrack coupler is that the surface magnetic field H_s will increase with respect to the regular one, especially in the neck of the coupler, as illustrated in Fig. 8. The maximum H_s is about 456 kA/m at target operating power, which is about 20% higher than the regular one. Using Eq. (3), the maximum temperature rise due to pulsed heating effect is about 28 °C, which is within a safe range to avoid unnecessary increases in BDR.

The performance of racetrack couplers on emittance growth suppression is validated through beam dynamics simulation. Three-dimensional field maps of XT72 with ether regular or racetrack couplers are simulated in CST Studio Suite® F-solver and then imported into General Particle Tracer® (GPT) for beam dynamics simulation. The results of emittance evolution at different z position of the entire VIGAS beamline are shown in Fig. 9. The primary parameters of the simulation are listed in Table V. All parameters and simulation settings are the same except for the fields in X-band structures. Therefore, the effect of quadrupole field components in the couplers can be clearly analyzed. The emittance using racetrack couplers are 0.39 μm compared to 0.42 μm when using regular couplers, representing about an 8% improvement.

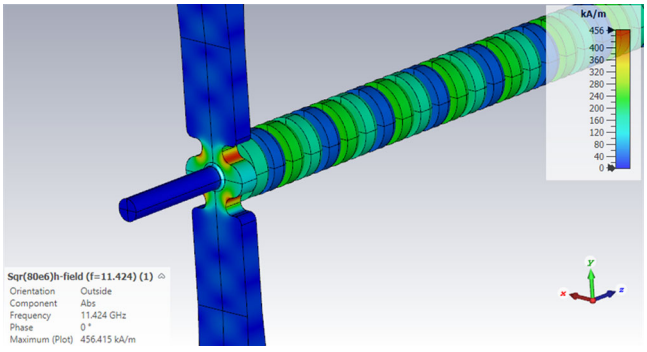

FIG. 8. Surface magnetic field distribution on the racetrack coupler.

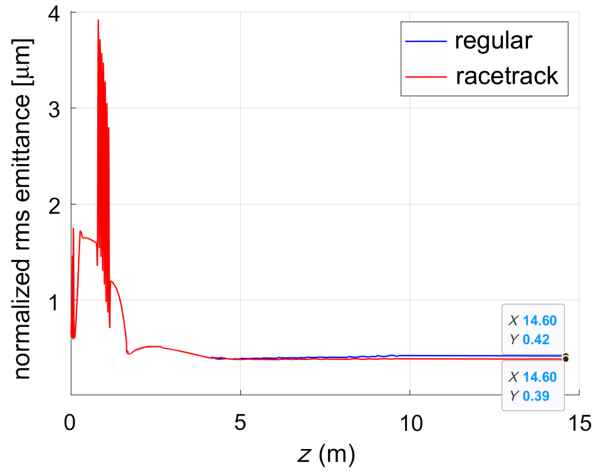

FIG. 9. Evolution of emittance versus position z is shown in two cases: one where all the X-band structures use regular couplers, and the other where racetrack couplers are used instead.

Both the calculation of multipole field components from rf simulations and the emittance calculation from beam dynamics simulations demonstrate that the racetrack coupler design is a superior option for our structure.

C. Wakefield effect analysis

Wakefields can be categorized as longitudinal and transverse wake. The longitudinal wakefield is proportional to the square of frequency ($w_{\parallel} \propto \omega^2$), while the transverse wakefield is proportional to the cube of frequency ($w_{\perp} \propto \omega^3$) [38]. Therefore, it is important to consider the wakefield effect of X-band structures due to their small beam apertures. Additionally, wakefield effects can also be classified as long range and short range. The short-range wakefield mainly affect the drive bunch itself, while the long-range wakefield acts on the bunch trailing behind the drive one. Since the repetition frequency of VIGAS is 10 Hz, the separation between a drive and a trailing bunch is significant enough that the long-range wakefield effect can be ignored, and we only need to consider the short-range wakefield effect for XT72.

TABLE V. Primary parameters in the beam dynamics simulation.

Parameters	Value
Laser pulse length (ps)	7.27
Laser transverse rms size (mm)	0.2
Electron bunch charge (pC)	200
Thermal emittance [μm/mm(rms)]	0.9
Photoinjector gradient (MV/m)	100
Sol1 strength (T)	0.2015
Buncher gradient (MV/m)	36
S acc gradient (MV/m)	27
Sol2 strength (T)	0.2075
X acc gradient (MV/m)	80

In one-dimension model, the wake potential (W_p) can be calculated from the convolution of wake function (w, the wake potential corresponding to a point charge) with the charged bunch density, as expressed by Eq. (4)

$$W_p(z) = \frac{1}{Q_{\text{tot}}} \int_{-\infty}^{\infty} w(z-\tau)\rho(\tau)d\tau, \tag{4}$$

where Q_{tot} is the total charge of the bunch, and $\rho(z)$ is the charge density distribution.

Generally, deriving the analytical expression for the wake functions of a structure is not easy, it is approximately expressed as a superposition of many eigenmodes of the structure [39,40]. Here we present a numerical method to deduce the wake function of an impedance structure. The procedure is introduced as follows. First, the XT72 three-dimension model is built in CST Studio Suite® wakefield solver, then the longitudinal and transverse wake potential can be numerically simulated. Then the wake function can be derived by the following Eq. (5):

$$w(z) = \mathcal{F}^{-1}\left[\frac{Q_{\text{tot}}\mathcal{F}[W_p(z)]}{\mathcal{F}[\rho(z)]}\right], \tag{5}$$

where $\mathcal{F}$ denotes the Fourier transformation symbol, and $\mathcal{F}^{-1}$ is the inverse process. Finally, the derived wake function is applied into General Particle Tracer® (GPT) wakefield element for beam dynamic simulation. Using this method, the wakefield effect on the beam emittance and energy spread could be analyzed.

Figure 10(a) illustrates the wake potential simulation settings in CST. The drive beam charge is 1 nC with 1.5 mm rms length. The cut-off frequency is as high as 68.2 GHz, which covers the fifth harmonic mode of 11.424 GHz. Figures 10(b)–10(d) are the wake potential simulation results. The longitudinal wakefield is obtained by setting the drive bunch on axis, while X and Y transverse wakefields are calculated by setting the drive bunch with an off-axis 1 and 1.5 mm, respectively. Since transverse wake function is proportional to the offset, the specific off-axis value does not matter, as it will be normalized during the calculation of the transverse wake function.

Substituting the wake potential data in Figs. 10(b)–10(d) and the drive bunch density into Eq. (5), the longitudinal and transverse wake function can be derived and as shown in Fig. 11. The wake function is truncated to 0.4 m because only the short-range wakefield is taken into consideration. A quick method to examine the validation of this result is to roughly calculate the fundamental wakefield amplitude using the analytical equation in Wangler's book [38]. The amplitude is $\frac{\omega}{2}\frac{r}{Q_0}$, substituting the parameters of XT72 in Table II, the result is about 500 V/pC, which

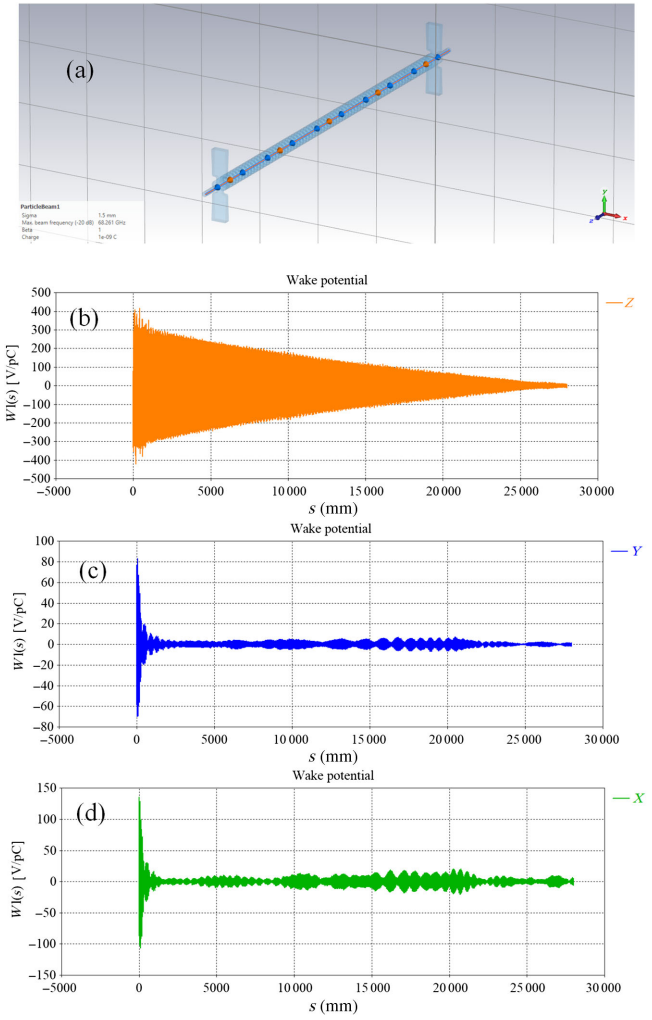

FIG. 10. Wake potential simulation in CST. (a) Simulation model and settings in CST. (b) Longitudinal wake potential. (c) Y-transverse wake potential with drive beam 1-mm off axis in Y direction. (d) X-transverse wake potential with drive beam 1.5-mm off axis in X direction.

is at the similar level of result in Fig. 11(a). It demonstrates that the results in Fig. 11 is reasonable.

Importing the data of Fig. 11 into GPT's wakefield element, the wakefield effect can be calculated in the beam dynamics simulation. Figure 12 indicates the emittance results with and without wakfield. From this figure, we observe that the emittance increases by approximately 10% due to the wakefield effect but still meets the required criteria. Figure 13 illustrates the energy spread with and without wakefield, and the result indicates that the influence is less than 1%, suggesting that it could be ignored. This indicates that the emittance is more sensitive to the wakefield effect in our structure. However, the value remains acceptable and meets the required emittance for the VIGAS project.

A short summary for this section, we first discuss the rf design of XT72, highlighting its maximum surface electric

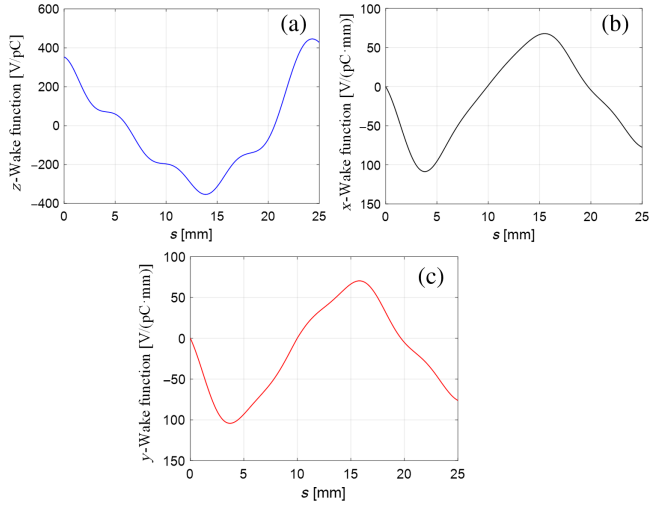

FIG. 11. Wake function of XT72. (a) Longitudinal wake function. (b) X-transverse wake function. (c) Y-transverse wake function.

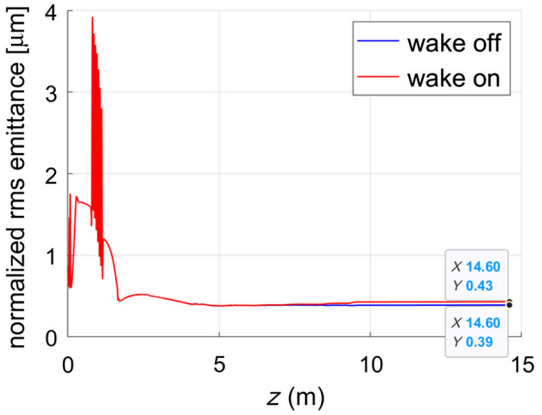

FIG. 12. Wakfield effect on emittance.

field and modified Poynting factor, which are lower than those of XC72 under operational conditions. Second, we examine the advantages of employing a racetrack coupler, providing both discussion and demonstration. Finally, we calculate the wakefield of XT72 and analyze its impact on beam dynamics. These comprehensive designs lay the groundwork for fabricating an improved X-band structure for the VIGAS project.

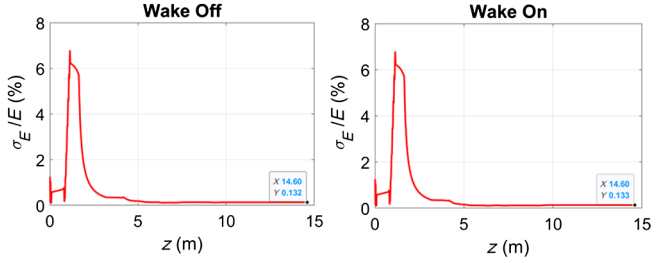

FIG. 13. Wakefield effect on energy spread. (a) With wakefield. (b) Without wakefield.

FIG. 14. Cells of XT72#1 before brazing (up) and structure after brazing (down).

III. FABRICATION AND TUNING

The bowl-shape regular cells are machined and the couplers are milled. All the dimensions tolerance are within 5 μm, and the surface roughness is less than 0.1 μm. The pictures of cells of XT72#1 before and after brazing is shown in Fig. 14.

Tuning of XT72#1 was performed using a 4-port VNA, and the on-axis field was measured using the nonresonant perturbation bead-pull method [41]. Then the detuning of each cell can be derived from the bead-pull data and local reflection [42] using Eq. (6). Where the ΔS_{11} denotes the reflection variation between with and without the bead, the E_n represents the electric field on axis in the nth cell, $\Gamma_{11}^{(n)}$ refers the local reflection in the nth cell, φ is the phase advance per cell, and Δf_n is the detuning frequency in the nth cell:

$$\begin{cases} {E_n}^2 \propto \Delta S_{11} \\ \Gamma_{11}^{(n)} = \frac{2E_n \cos\varphi - (E_{n-1}+E_{n+1})}{E_{n-1} - E_n e^{-j\varphi}} \\ \Delta f_n = \frac{f}{\varphi} \frac{\mathrm{Imag}[\Gamma_{11}^{(n)}]}{v_g/c} \end{cases}. \tag{6}$$

The results of the first XT72 tuning are depicted in Fig. 15. Before tuning, there is a strong standing wave inside the structure and the phase advance per cell is far from 120°. As illustrated in Figs. 15(c) and 15(d), the field balance and phase after tuning are improved and meet the requirements of the $2\pi/3$ constant gradient structure. The phase advance per cell is $120° \pm 1.4°$ from Fig. 15(e).

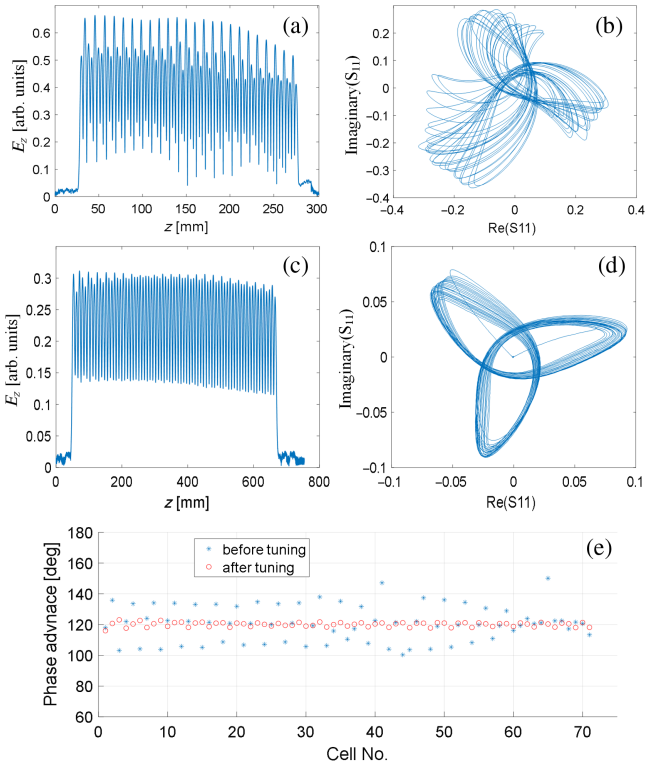

FIG. 15. Tuning results. (a), (b) Amplitude and phase of field before tuning. (c), (d) Amplitude and phase of field after tuning. (e) Comparison of phase advance per cell between before tuning and after tuning.

Figure 16 illustrates the S parameters after tuning. At the working frequency, the reflection S_{11} is −28 dB and the transmission S_{21} is −4.45 dB, which are well matched with simulation values of −4.38 dB. The filling time can also be calculated from the S parameters [28], as expressed in Eq. (7), where $\varphi[S_{21}]$ denotes the phase of S_{21}, and ω_0 is the working frequency. The phases of S_{21} from the measurement and simulation are plotted together in Fig. 17, and they match each other very well. The filling time calculated

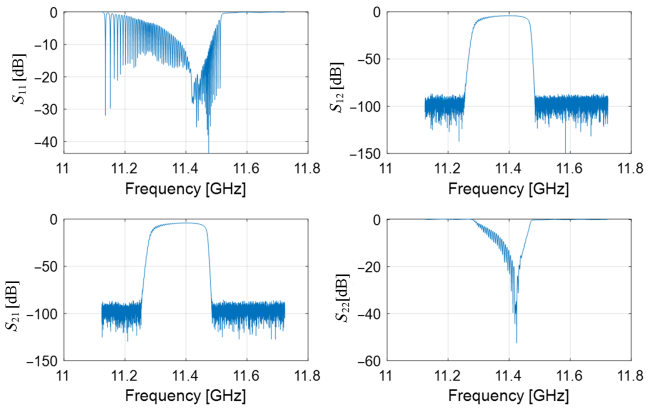

FIG. 16. S parameters after tuning.

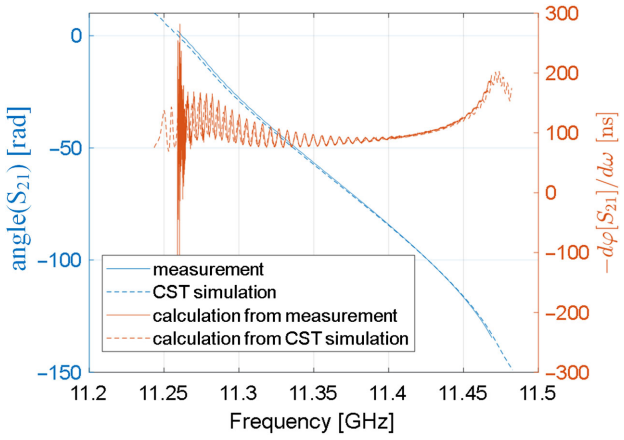

FIG. 17. Phase of S_{21} and filling time from calculation.

from the phase of S_{21} from measurement is 98.3 ns, which agrees well with the single cell calculation in Table II:

$$t_f = -\frac{d\varphi[S_{21}]}{d\omega}\bigg|_{\omega_0}. \tag{7}$$

The group velocity can be derived from filling time by $v_g = \frac{L}{tf} = 2.1\%c$. The quality factor can be obtained by using Eq. (8):

$$Q = \frac{\omega_0}{2\alpha v_g}, \tag{8}$$

where α is the attenuation factor and can be derived from the S_{21} magnitude. Substituting the working frequency, group velocity, and attenuation faction into Eq. (8), the quality factor result is 6886, which is closely aligns with the value of 6937 obtained from the CST entire structure simulation and also matched with the single cell simulation results in Table I.

The results of tuning and low-power rf tests demonstrate that the rf properties of the structure meet the design requirements, indicating that it is ready for high-power testing.

IV. HIGH-POWER TEST

The high-power conditioning of the first X-band constant gradient structure (XT72) was conducted at Tsinghua high-power test stand for X-band (TPOT-X) [43]. The power source is a CPI VKX8311B Klystron capable of generating 50-MW power with a pulse width of 1.5 μs and a repetition rate of 40 Hz, operating at a frequency around 11.4 GHz. Figure 18 depicts the setup of high-power test stand.

The power generated from the Klystron is boosted by the pulse compressor by a factor of 4, and the pulse width is compressed by a factor of 10. Therefore, the maximum peak power injected into the test stand can reach 200 MW

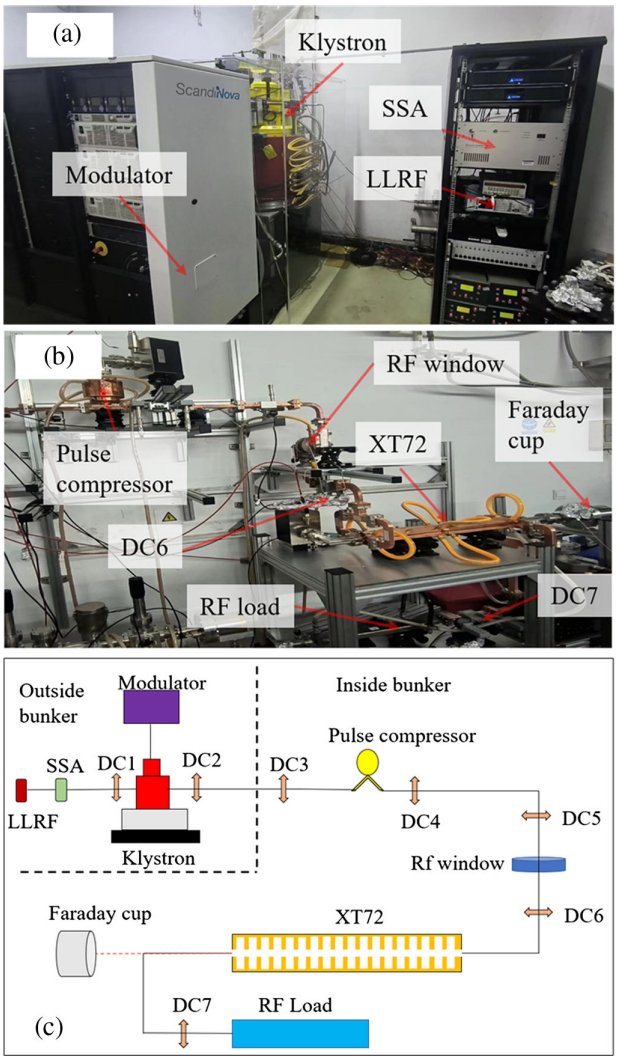

FIG. 18. Setup of high-power test stand. (a) rf room outside the bunker. (b) Test stand inside bunker. (c) Schematic of the setup. Abbreviation: LLRF: low-level rf, SSA: solid state amplifier, and dc: directional coupler.

with a 150-ns pulse width. The power transmitting out of the device under test is absorbed by an X-band high-power rf load, which is scaled from S-band version [44]. Directional couplers (DC6 and DC7) located at the entrance and exit monitor the transmission and reflection rf power, used to analyze the test structure's conditioning status. Other directional couplers (DC1–DC4) are used to monitor the output power of SSA, Klystron, and pulse compressor. A Faraday cup is installed at the exist of the device under test for the dark current recording. A high-power rf window separates the test structure from the upstream, eliminating the need to break the upstream vacuum when switching the device under test.

During the rf conditioning, the transmission, and reflection power waveforms from DC6 and DC7 are recorded every 5 s. The vacuum level and dark current signals are also monitored by the system. The conditioning strategy is

described as follows: the power level increasing period is set to 60 s with a rest time of 30 s. During the 60-s conditioning period, if no breakdown occurs, the power level is increased by 0.1 MW. However, in the event of a breakdown, the rf is turned off for 30 s to evacuate the structure, and the power level is decreased by 0.1 MW. There are thresholds for the reflection signal from DC6 at the entrance of the device under test, the vacuum level, and the dark current. If any of them exceeds the set thresholds, the interlock is triggered, and an event of breakdown is recognized and recorded.

The high-power test results of first XT72 are illustrated in Fig. 19, along with the XC72 results from [28] at right. Figures 19(i) and 19(ii) indicate a normal waveform of the input, the reflection power from DC6 at the entrance of the structure and the transmission power from the exit of the structure. The gradient in the figures are calculated from the input power waveform using Eq. (2) with the quality factor (Q) from measurement results. The waveforms in Figs. 19(i) and 19(ii) were captured at BDR level of 10^{-4}/pulse/m, the peak power and gradient of XT72#1 were measured as 76.1 MW and calculated as 81.0 MV/m, while for XC72 they were 78.6 MW and 78.7 MV/m, respectively. The reason that the peak power of XT72#1 needed for 80 MV/m in Fig. 19(i) is lower than that of in Fig. 3 is because of the different pulse shapes. The ideal pulse shape output from a pulse compressor is exponentially decaying, however, in the experiment, we increased the phase reverse time and applied the amplitude modulation for the input pulse, thus a relative flat pulse was generated compared to the ideal case. As stated in Sec. II A, constant gradient structure prefers a pulse with a flat top.

Figures 19(iii) and 19(vi) depict the peak power, breakdown numbers, pulse width, and gradient during the conditioning history. Data points from XT72#1 appear denser because we use more data samples from the conditioning history compared to those from XC72. Both structures underwent approximately 17 million pulses and required around 120 h for high-power conditioning. Obviously, the XT72#1 reached the goal gradient more quick than the XC72. The breakdown numbers are at a similar level, around 9000. We believe that by making the conditioning strategy slightly less aggressive, such as by extending the duration of each power step, the number of breakdowns could be reduced. Figures 19(v)–19(xii) show the maximum surface electric field, maximum modified Poynting factor, and maximum pulse heating of each pulse during the conditioning history. These three quantities are calculated from input power pulse. The performance of XT72 is clearly superior to that of XC72. Detailed numerical values of these quantities are listed in Table VI for comparison.

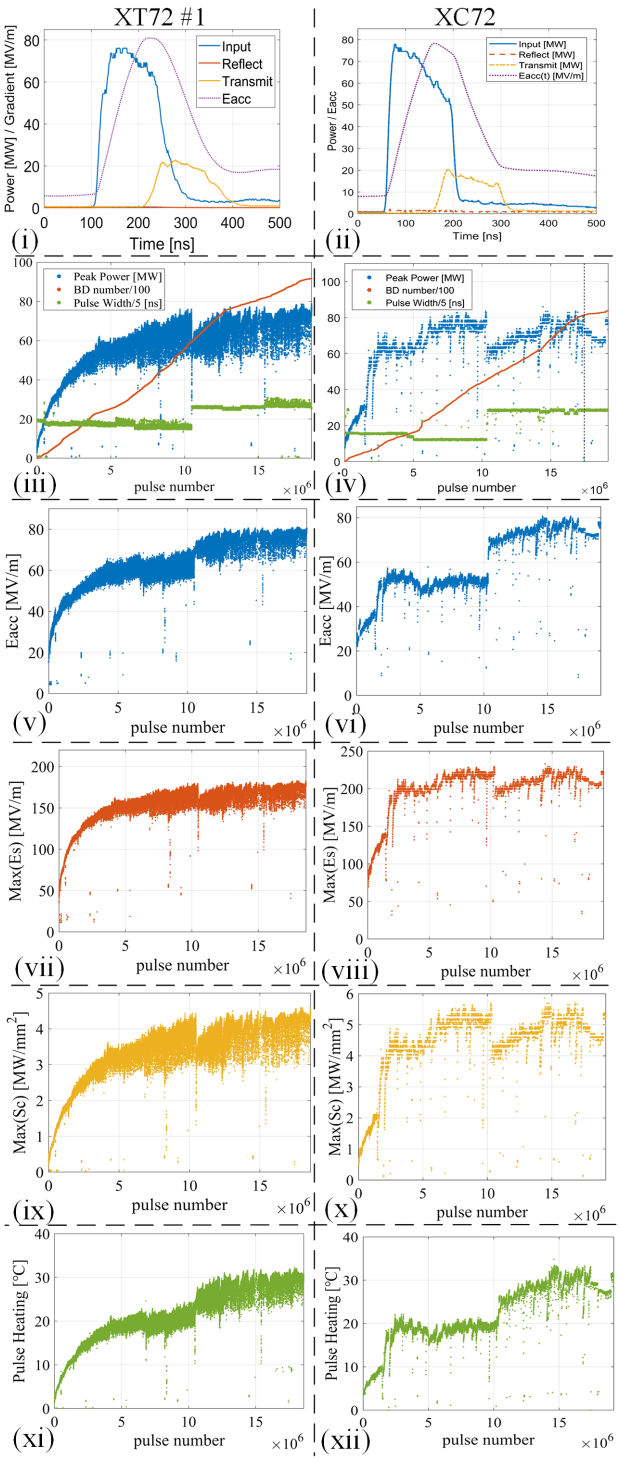

FIG. 19. Comparison of high-power test results between XT72#1 (left) and XC72 (right). (i), (ii) Input power (blue line), reflection power (red line), transmission power (yellow line), and gradient (Eacc, dotted purple line). (iii)–(xii) Conditioning history of peak power, breakdown (BD) numbers, pulse width, gradient (Eacc), maximum surface electric field [Max(Es)], maximum modified Poynting factor [Max(Sc)], and maximum pulse heating.

TABLE VI. Comparison of XT72 and XC72 on maximum surface electric field E_s, modified Poynting factor S_c, and temperature rising due to pulsed heating in the conditioning history.

Properties	XT72	XC72
Max(E_s) (MV/m)	182	225
Max(S_c) (MW/mm^2)	4.6	5.5
Max (ΔT) (°C)	32.0	34.5

The locations where breakdowns occur can also be estimated using the approach mentioned in [28,45], here we briefly repeat its processing procedure. When a breakdown occurs in the structure during the input pulse, the portion of the pulse preceding the breakdown timestamp continues to transmit through the structure. Consequently, the width of the transmitted pulse (t_{tr}) leaving the structure indicates the timestamp of the breakdown occurring in the input pulse. The latter portion of the input pulse will be reflected toward the input coupler and captured by the directional coupler as the reflection signal. The time separation between the rising edges of the input and reflection pulses (t_{re}) represents the round-trip time traveled by the signal. Therefore, the location of the breakdown occurring from the input coupler can be calculated using the following equation:

$$\sum_{i=1}^{n} \frac{2L}{v_{g_i}} > t_{re} - t_{tr} \geq \sum_{i=1}^{n-1} \frac{2L}{v_{g_i}}, \tag{9}$$

where L is the single cell length, v_{g_i} represents the group velocity of the ith cell, and n is the cell index number where breakdown happens.

In Fig. 20, we present two instances of breakdown event occurring in XT72#1: one at the front part of the structure and the other at the rear part. Apparently, the breakdown location information can be derived from t_{re} and t_{tr}.

By applying the approach introduced above, we can count the numbers of breakdown occurring at each cell during the conditioning history, as shown in Fig. 21. From the comparison, it is observed that breakdowns have a high probability of occurring at the first several cells of the constant impedance structure (XC72), as the electric field

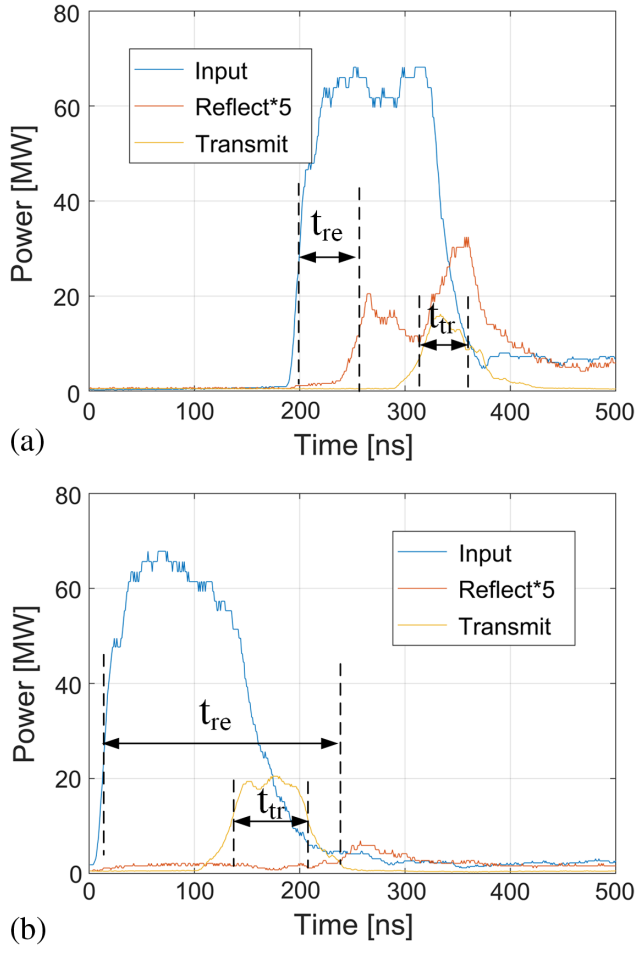

FIG. 20. Breakdown instances of XT72#1. (a) The breakdown occurs at the front part of the structure. (b) The breakdown occurs at the rear part of the structure.

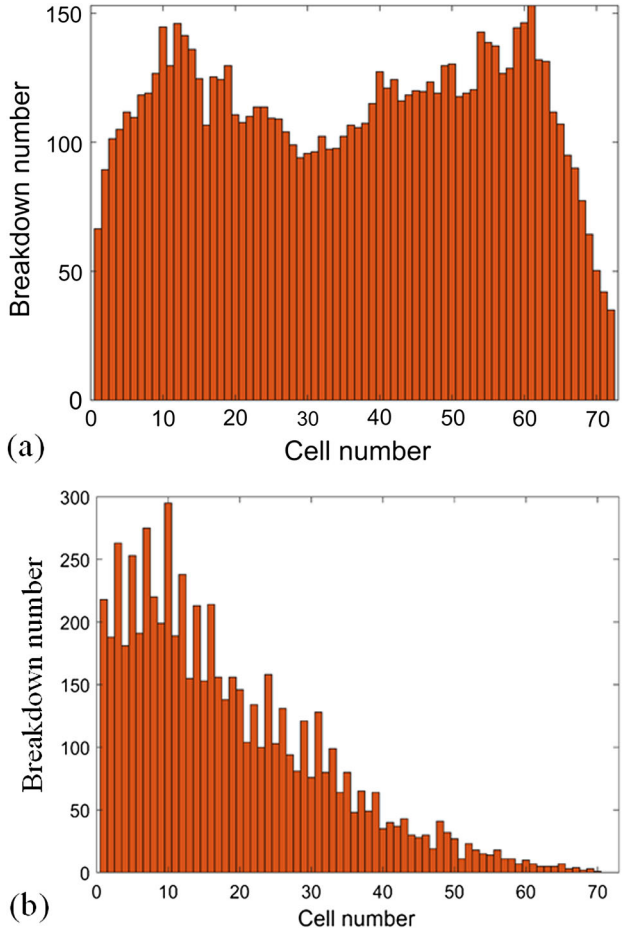

FIG. 21. Breakdowns distribution in the (a) constant gradient structure XT72#1 and (b) constant impedance structure XC72.

decreases from input end to output end in such a structure. However, the breakdown distribution is more uniform in the constant gradient structure (XT72) compared to XC72, corresponding to a nearly flat electric field distribution as shown in Fig. 15(c).

The high-power test results demonstrate that the new constant gradient structure (XT72) performs better than the constant impedance structure (XC72). XT72 reached 81.0 MV/m at a lower BDR of 1.5×10^{-4} within 17 millions conditioning pulses. The improvement is attributed to the reduction of the electric and magnetic field in the structure at the target gradient level, resulting in a more uniform probability of a breakdown event occurring in each cell. This uniformity benefits the conditioning process, resulting in a lower breakdown rate (BDR) for XT72 compared to XC72 at the same gradient level. In conclusion, XT72 has been demonstrated to be superior and meets the requirements of the VIGAS project. As a result, the other five X-band accelerating structures will adopt the same design for fabrication.

V. SUMMARY

This paper presents the design, fabrication, and testing of an X-band constant gradient structure for the VIGAS project at Tsinghua University. The high-power test results indicate that this structure outperforms previous constant impedance structure XC72, reaching a gradient of 81.0 MV/m compared to 78.7 MV/m within 17 million pulse conditioning at a BDR level of 10^{-4}/pulse/m. The successful development of the first constant gradient structure demonstrates its superiority for VIGAS main accelerators. Other X-band high-gradient structures in the world, such as CERN TD26R05CC, TD24R05, KEK TD24R05-#2, and TD24R05-#4 [32], took more than 100 million pulses for conditioning to reach the gradient of 80 MV/m with a BDR of 10^{-6}/pulse/m. XT72#1 took much less pulses for conditioning but a higher BDR because we took an aggressive conditioning strategy due to the VIGAS project tight schedule and its loose BDR requirement. Further conditioning will be conducted on beamline to achieve a gradient above 80 MV/m with a target BDR at the level of 10^{-5}/pulse/m. Subsequent XT72 structures (#2 to #6) have been fabricated and are undergoing brazing and exhausting. We plan to complete conditioning of these structures by the end of this year and conduct a full comparison and analysis of the conditioning history for all six structures.

ACKNOWLEDGMENTS

We gratefully acknowledge the support of the National Natural Science Foundation of China (NSFC Grant No. 12027902). We extend our sincere appreciation to the senior engineers at the Corporation Limited of Beijing Huaqingjia High Energy Electron Technology for their invaluable assistance with fabricating and brazing work, including Jiaqi Qiu, Chuanqing Wang, Yunsheng Han, Jingzhong Xiao, and others. We also wish to express our gratitude to the students at Tsinghua Accelerator Laboratory, including An Li, Chongnan Shi, Hao Wang, Kede Jie, Zhengkai Wang, who contributed to the high-power test experiment. Their contributions were invaluable, and we sincerely thank all participants for their dedication and support.

[1] D. Habs and U. Köster, Appl. Phys. B **103**, 501 (2011).
[2] F. Hartemann, H. Baldis, A. Kerman, A. Le Foll, N. Luhmann Jr., and B. Rupp, Phys. Rev. E **64**, 016501 (2001).
[3] R. Hajima, T. Hayakawa, N. Kikuzawa, and E. Minehara, J. Nucl. Sci. Technol. **45**, 441 (2008).
[4] M. Jentschel, F. Albert, T. Buslaps, U. Friman-Gayer, V. Honkimaki, L. Mertes, A. J. Pollitt, P. Mutti, N. Pietralla, and C. Barty, Appl. Opt. **61**, C125 (2022).
[5] M. Jacquet and P. Suortti, Phys. Med. **31**, 596 (2015).
[6] P. Walter, A. Variola, F. Zomer, M. Jaquet, and A. Loulergue, C. R. Phys. **10**, 676 (2009).
[7] I. Sakai, T. Aoki, K. Dobashi, M. Fukuda, A. Higurashi, T. Hirose, T. Iimura, Y. Kurihara, T. Okugi, T. Omori *et al.*, Phys. Rev. ST Accel. Beams **6**, 091001 (2003).
[8] K. Dupraz, M. Alkadi, M. Alves, L. Amoudry, D. Auguste, J.-L. Babigeon, M. Baltazar, A. Benoit, J. Bonis, J. Bonenfant *et al.*, Phys. Open **5**, 100051 (2020).
[9] B. Hornberger, J. Kasahara, M. Gifford, R. Ruth, and R. Loewen, in *Proceedings of the Advances in Laboratory-Based X-Ray Sources, Optics, and Applications VII* (SPIE, San Diego, CA, 2019), Vol. 11110, p. 1111003, https://www.spiedigitallibrary.org/conference-proceedings-of-spie/11110/1111003/A-compact-light-source-providing-high-flux-quasi-monochromatic-tunable/10.1117/12.2527356.full.
[10] E. Eggl, M. Dierolf, K. Achterhold, C. Jud, B. Günther, E. Braig, B. Gleich, and F. Pfeiffer, J. Synchrotron Radiat. **23**, 1137 (2016).
[11] K. Dupraz, K. Cassou, N. Delerue, P. Fichot, A. Martens, A. Stocchi, A. Variola, F. Zomer, A. Courjaud, E. Mottay *et al.*, Phys. Rev. ST Accel. Beams **17**, 033501 (2014).
[12] S. Gales, K. Tanaka, D. Balabanski, F. Negoita, D. Stutman, O. Tesileanu, C. Ur, D. Ursescu, I. Andrei, S. Ataman *et al.*, Rep. Prog. Phys. **81**, 094301 (2018).
[13] C. Tang, W. Huang, R. Li, Y. Du, L. Yan, J. Shi, Q. Du, P. Yu, H. Chen, T. Du *et al.*, Nucl. Instrum. Methods Phys. Res., Sect. A **608**, S70 (2009).
[14] Z. Chi, L. Yan, Y. Du, Z. Zhang, W. Huang, H. Chen, and C. Tang, Nucl. Instrum. Methods Phys. Res., Sect. B **402**, 364 (2017).
[15] Y. Du, L. Yan, J. Hua, Q. Du, Z. Zhang, R. Li, H. Qian, W. Huang, H. Chen, and C. Tang, Rev. Sci. Instrum. **84**, 053301 (2013).
[16] D. Yingchao, C. Han, Z. Hongze, G. Qiang, T. Qili, C. Zhijun, Z. Zhi, Z. Hao, S. Jiaru, Y. Lixin *et al.*, High Power Laser Particle Beams **34**, 104010 (2022).

[17] Q. Gao, Progress of accelerator system for the VIGAS project in Tsinghua University, in *International Workshop on Breakdown Science and High Gradient Technology, HG-2022*, https://indico.cern.ch/event/1080222/contributions/4844198/attachments/2445909/4190959/HG2022_Tsinghua_QG_upload.pdf (2022).

[18] J. Shi, Very compact inverse Compton scattering gamma ray source (VIGAS) at Tsinghua University, in *Workshop on Compact Light Complementary Use and Opportunities* (2021).

[19] L. Zheng, Y. Du, Z. Zhang, H. Qian, L. Yan, J. Shi, Z. Zhang, Z. Zhou, X. Wu, X. Su *et al.*, Nucl. Instrum. Methods Phys. Res., Sect. A **834**, 98 (2016).

[20] X.-C. Lin, H. Zha, J.-R. Shi, L.-Y. Zhou, Y.-F. Liang, J. Gao, Q. Gao, H.-B. Chen, and C.-X. Tang, Nucl. Sci. Tech. **33**, 147 (2022).

[21] H. Chen, L. Yan, Q. Tian, Z. Lin, D. Wang, C. Cheng, J. Shi, H. Zha, Y. Du, H. Chen *et al.*, Phys. Rev. Accel. Beams **22**, 053403 (2019).

[22] A. Degiovanni, W. Wuensch, and J. G. Navarro, Phys. Rev. Accel. Beams **19**, 032001 (2016).

[23] W. Kilpatrick, Rev. Sci. Instrum. **28**, 824 (1957).

[24] A. Grudiev and W. Wuensch, Design of the CLIC main linac accelerating structure for CLIC conceptual design report, Technical Reports No. EuCARD-CON-2010-073, No. CERN-ATS-2010-212, 2010, https://cds.cern.ch/record/1346987/.

[25] X. Wu, H. Zha, J. Shi, H. Chen, T. Abe, T. Higo, and S. Matsumoto, Phys. Rev. Accel. Beams **22**, 031001 (2019).

[26] R. Assmann, M. Weikum, T. Akhter, D. Alesini, A. Alexandrova, M. Anania, N. Andreev, I. Andriyash, M. Artioli, A. Aschikhin *et al.*, Eur. Phys. J. Special Topics **229**, 3675 (2020).

[27] X. Huang, W. Fang, Q. Gu, and Z. Zhao, Nucl. Instrum. Methods Phys. Res., Sect. A **854**, 45 (2017).

[28] X.-C. Lin, H. Zha, J.-R. Shi, Q. Gao, J.-Y. Liu, L.-Y. Zhou, J. Gao, H.-B. Chen, and C.-X. Tang, Nucl. Sci. Tech. **33**, 147 (2022).

[29] A. Grudiev, S. Calatroni, and W. Wuensch, Phys. Rev. ST Accel. Beams **12**, 102001 (2009).

[30] A. Grudiev, S. Calatroni, and W. Wuensch, Phys. Rev. ST Accel. Beams **14**, 099902 (2011).

[31] J.-Y. Liu, J.-R. Shi, H. Zha, A. Grudiev, P. Wang, Y.-C. Du, and H.-B. Chen, Nucl. Sci. Tech. **31**, 107 (2020).

[32] W. L. Millar, Operation of multiple accelerating structures in an x-band high-gradient test stand, PhD thesis, Lancaster University, United Kingdom, 2021.

[33] V. A. Dolgashev, in *Proceedings of the 2003 Particle Accelerator Conference* (IEEE, New York, 2003), Vol. 2, pp. 1267–1269.

[34] D. P. Pritzkau and R. H. Siemann, Phys. Rev. ST Accel. Beams **5**, 112002 (2002).

[35] L. Laurent, S. Tantawi, V. Dolgashev, C. Nantista, Y. Higashi, M. Aicheler, S. Heikkinen, and W. Wuensch, Phys. Rev. ST Accel. Beams **14**, 041001 (2011).

[36] C. Adolphsen, W. Baumgartner, K. Jobe, F. Le Pimpec, R. Loewen, D. McCormick, M. Ross, T. Smith, J. Wang, and T. Higo, in *Proceedings of the 2001 Particle Accelerator Conference, PACS-2001* (IEEE, New York, 2001), Vol. 1, pp. 478–480.

[37] M. Chae, J. Hong, Y. Parc, I. S. Ko, S. Park, H. Qian, W. Huang, and C. Tang, Phys. Rev. ST Accel. Beams **14**, 104203 (2011).

[38] T. P. Wangler, *RF Linear Accelerators* (John Wiley & Sons, Hoboken, NJ, 2008).

[39] Q. Gao, G. Ha, C. Jing, S. Antipov, J. Power, M. Conde, W. Gai, H. Chen, J. Shi, E. Wisniewski *et al.*, Phys. Rev. Lett. **120**, 114801 (2018).

[40] Q. Gao, J. Shi, H. Chen, G. Ha, J. G. Power, M. Conde, and W. Gai, Phys. Rev. Accel. Beams **21**, 062801 (2018).

[41] C. W. Steele, IEEE Trans. Microwave Theory Tech. **14**, 70 (1966).

[42] J. Shi, A. Grudiev, and W. Wuensch, Nucl. Instrum. Methods Phys. Res., Sect. A **704**, 14 (2013).

[43] M. Peng, J. Shi, P. Wang, W. Gai, D. Cao, Y. Jiang, and J. Liu, in *9th International Particle Accelerator Conference IPAC-2018* (2018), pp. 3999–4001.

[44] X. Meng, J. Shi, H. Zha, Q. Gao, Z. Liu, J. Liu, Y. Jiang, P. Wang, H. Chen, and J. Qiu, Nucl. Instrum. Methods Phys. Res., Sect. A **927**, 209 (2019).

[45] W. Wuensch, A. Degiovanni, S. Calatroni, A. Korsbäck, F. Djurabekova, R. Rajamäki, and J. Giner-Navarro, Phys. Rev. Accel. Beams **20**, 011007 (2017).